COPPE
UFRJ

**Instituto Alberto Luiz Coimbra de
Pós-Graduação e Pesquisa de Engenharia**

DESIGN AND OPTIMIZATION OF A BIAS FLAP ACTUATOR DRIVEN BY 1-D ELECTRO-THERMO-MECHANICALLY COUPLED SHAPE MEMORY ALLOY ACTUATORS

Pedro Batista Camara Leal

Dissertação de Mestrado apresentada ao Programa de Pós-graduação em Engenharia Mecânica, COPPE, da Universidade Federal do Rio de Janeiro, como parte dos requisitos necessários à obtenção do título de Mestre em Engenharia Mecânica.

Orientador: Marcelo Amorim Savi

Rio de Janeiro
Agosto de 2016

DESIGN AND OPTIMIZATION OF A BIAS FLAP ACTUATOR DRIVEN BY 1-D ELECTRO-THERMO-MECHANICALLY COUPLED SHAPE MEMORY ALLOY ACTUATORS

Pedro Batista Camara Leal

DISSERTAÇÃO SUBMETIDA AO CORPO DOCENTE DO INSTITUTO ALBERTO LUIZ COIMBRA DE PÓS-GRADUAÇÃO E PESQUISA DE ENGENHARIA (COPPE) DA UNIVERSIDADE FEDERAL DO RIO DE JANEIRO COMO PARTE DOS REQUISITOS NECESSÁRIOS PARA A OBTENÇÃO DO GRAU DE MESTRE EM CIÊNCIAS EM ENGENHARIA MECÂNICA.

Examinada por:

_____
Prof. Marcelo Amorim Savi, D.Sc.

_____
Prof. XXX, D.Sc.

_____
Prof. XXX, D.Sc.

RIO DE JANEIRO, RJ – BRASIL
AGOSTO DE 2016

Para Tita.

Agradecimentos

EU e ela.

Resumo da Dissertação apresentada à COPPE/UFRJ como parte dos requisitos necessários para a obtenção do grau de Mestre em Ciências (M.Sc.)

DESIGN AND OPTIMIZATION OF A BIAS FLAP ACTUATOR DRIVEN BY
1-D ELECTRO-THERMO-MECHANICALLY COUPLED SHAPE MEMORY
ALLOY ACTUATORS

Pedro Batista Camara Leal

Agosto/2016

Orientador: Marcelo Amorim Savi

Programa: Engenharia Mecânica

EU e nois.

Abstract of Dissertation presented to COPPE/UFRJ as a partial fulfillment of the requirements for the degree of Master of Science (M.Sc.)

XXX

Pedro Batista Camara Leal

August/2016

Advisor: Marcelo Amorim Savi

Department: Mechanical Engineering

With the increasing amount of works related to morphing wings, it has become relevant to validate current engineering models applied on wing geometries with actual experiments. This paper focuses on the characterization of shape memory alloy (SMA) springs and the modelling of a plain flap actuated by a combination of SMA and elastic springs. The SMA actuators are mechanically, electrically and thermally characterized. An electro-thermo-mechanical coupled Hartl-Lagoudas constitutive model is proposed and used for the Finite Element Analysis (FEA) of a 3D SMA spring or wire heated via an electrical potential difference. A 1D SMA Spring constitutive model is formulated and compared to the 3D and experimental results. An experimental set-up and analytical 2D rigid body flap are described. The elastic spring properties, the positioning of the springs/wire and the voltage are optimized to maximize the trailing edge displacement with the minimum transformation strain and voltage possible. These results are then compared to the displacement obtained from an experimental plain flap prototype.

Contents

List of Figures

List of Tables

Chapter 1

Introduction

As an essential aircraft component, flap actuators are compact, have a high fatigue life and are able to exert high forces. To exceed the limitations of modern actuators built out of traditional materials, new materials are necessary. However, the industry has not yet integrated these new materials because of their non-linear properties and sometimes unpredictable performance. Notwithstanding, researchers have thoroughly analysed and modelled a class of materials known as Shape Memory Alloys (SMA)[2]. It is the authors' belief that the level of SMA technology is now mature enough to develop new aerospace applications, including an SMA driven flap.

For aeronautical actuation applications, SMA components (i.e. wires, springs and ribbons) are proposed in lieu of other smart materials (i.e. piezoelectric, shape memory polymers and others) because they have high actuation stress, high actuation strain and thus high energy density [3]. Lagoudas et al. [1], Savi et al. [4] and other authors have proposed constitutive equations to model the properties of these components. The authors chose to use herein the Lagoudas et al. model because of experimental validation and an already available robust and optimized algorithm in Abaqus.[1]. Moreover, a electro-thermo-mechanical coupling is proposed via the martensite volume fraction.

Several works have proposed the use of SMA actuators for the development of morphing structures [5, 6]. However, the complexity of such mechanisms impedes their experimental validation. Others have applied SMA wires as actuators for control surfaces [7–9]. Nevertheless, there is a lack of validation of these mechanisms with numerical and experimental results. However, several works[7, 9–11] concluded that wires can be quite limiting for flap deflections. For higher stroke at the cost of providing less force, SMA springs can be used. Herein, both components will be used depending on the necessary force and displacement. The flap itself acts as a lever for magnifying the displacement for the SMA components.

SMA configurations to achieve linear motion are classified as either *bias* or *antagonistic*. The fist type consists of one SMA actuator acting against one bias spring. It

is characterized as having larger stroke, fast actuation during heating, but slow reset during cooling [12]. The second type consists of a pair of SMA actuators arranged antagonistically. Because one can control the motion in both directions actively, it has enhanced controllability. [13] A compact flap actuator necessitates high stroke, but does not require a fast retraction time. Inspired by previously existing actuator patents[14, 15] and by prototypes found in the literature[12, 16], a mechanism of two coaxial components, a passive spring and a SMA spring/wire, actuated by electrical heating was developed and considered herein.

The main challenges for SMA implementation include energy efficiency and fatigue [6]. The amount of thermal energy required for actuation is much larger than mechanical work output resulting in an efficiency of 10-15% for wires [3], but even worse for springs. Although fatigue is a serious mechanical problem, Kumar and Lagoudas [2] have reported that thermally-induced partial martensitic transformations cycles significantly extend the material's fatigue life. Therefore, to design a robust SMA mechanism with a considerable fatigue life and low energy consumption, the authors have focused on minimizing the necessary martensitic volume fraction and the voltage applied to the system.

1.1 Single actuated flap

Missing figure   Add CAD model and references to it
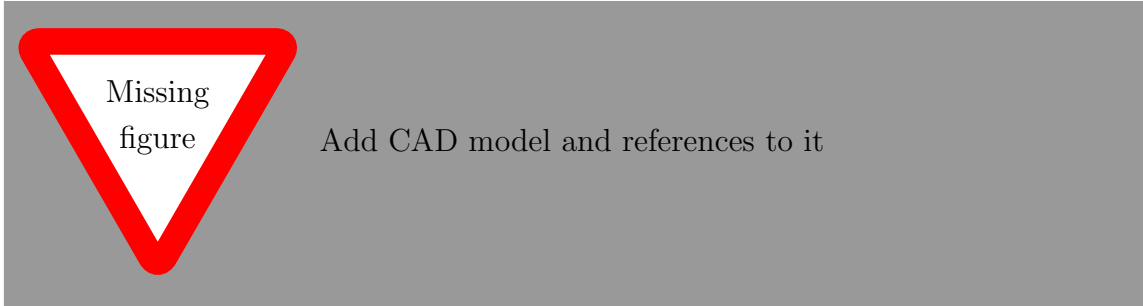
Figure 1a depicts the flap model herein studied. Other airfoils with higher efficiency (e.g. single-slotted flap, double-slotted flap and split flap) exist, but a plain flap geometry is utilized for simplicity[17]. The bias spring configuration is depicted in Fig. 1a and in more detail in Fig. 1b. The mechanism consists of an elastic compression and a martensite SMA spring/wire coaxially annexed to isolating Teflon fixtures. To avoid buckling, low slenderness ratio (l/D) for the compression spring is desirable[18]. Therefore, when utilizing a SMA spring, the elastic spring will be the external component (i.e. Fig 1b). If necessary, an articulated isolating acrylic layer was designed to prevent contact between both springs. The linear spring stiffness coefficient, K, must be high enough so that the SMA spring/wire is detwinned enough to obtain the necessary stroke. An Arduino micro-controller is

utilized to control the electrical potential heating the SMA component, to measure the temperature with thermocouples and to measure the flap displacement via an accelerometer.
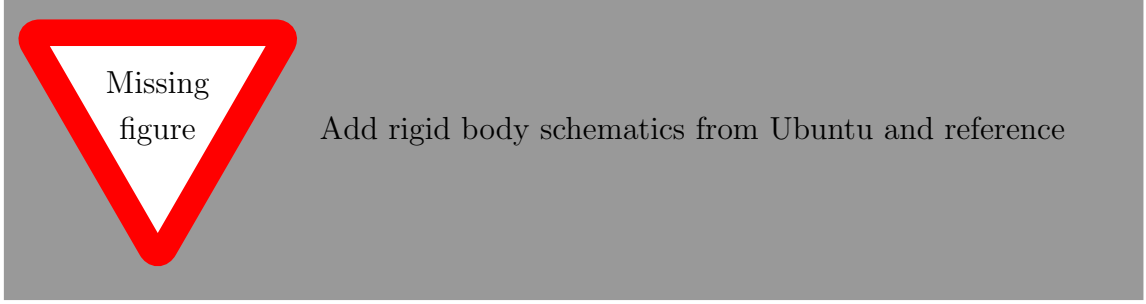
A 2D FEA flap model was developed, but due to the low stresses at the flap components, it was further simplified such that these components can be modelled as rigid bodies. If the coordinate system's origin is defined at the leading edge and the x-axis connects the leading edge to trailing edge, from figure **??**, we can find the following geometric relations:

$$l_{FJ} = \sqrt{(x_J - x_F)^2 + (y_J - y_F)^2} \qquad l_{JA} = \sqrt{(x_A - x_J)^2 + (y_A - y_J)^2} \qquad (1.1)$$

$$\delta = sin^{-1}\left(-\frac{l_{FA}^2 - l_{FJ}^2 - l_{JA}^2}{2l_{FJ}l_{JA}}\right) - tan^{-1}\left(\frac{x_J - x_F}{y_F - y_J}\right) - tan^{-1}\left(\frac{y_J - y_A}{x_A - x_J}\right) \qquad (1.2)$$

where the subscripts F, J and A correspond, respectively, to the attachment point of the springs on the Forwards component($\mathcal{F}$), of the Afterwards component ($\mathcal{A}$) on $\mathcal{F}$ and of the springs on $\mathcal{A}$; l_{ij} is the absolute length between points i and j; and δ is the flap deflection. If the final actuation length, l_{FA}, is known, δ is calculated with equation 1.2.

1.2   Multi-actuated flap

Chapter 2

Concepts and tools

2.1 Fundamental concepts

Although complicated geometries, most wings can be represented through a collection of geometric characteristics related to their cross-section (Figure **??**) or to their top view (Figure **??**). Here, the following geometric wing related concepts have been utilized:

- *Leading Edge*: the foremost edge of an airfoil section, usually the edge at the round-off end Also defined as the origin, e.g. the (0,0) point, of our coordinate system.

- *Trailing Edge*: the rearmost edge of an airfoil section, usually the edge at the sharp end of the airfoil.

- *Chord*: absolute distance from the leading edge to the trailing edge.

- ψ: nodes' coordinates along the *chord line* and normalized by the *chord*.

- ζ: nodes' coordinates normal of the *chord line* and normalized by the *chord*.

- *Camber Line*: line of points midway between the upper and lower surfaces.
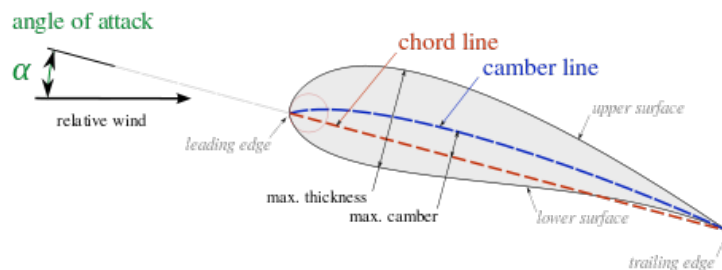
Figure 2.1: Representative airfoil depicting all relevant geometric definitions
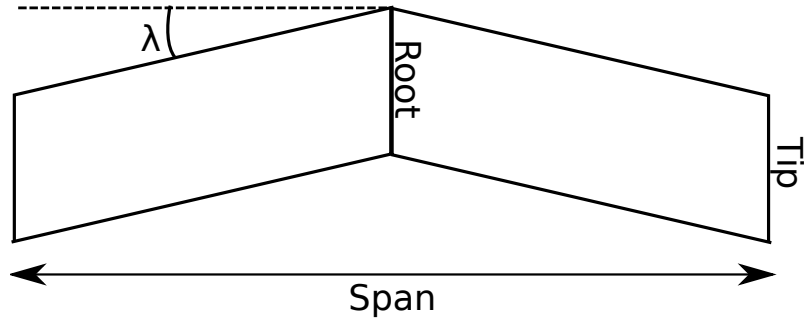
Figure 2.2: Representative wing depicting all relevant geometric definitions
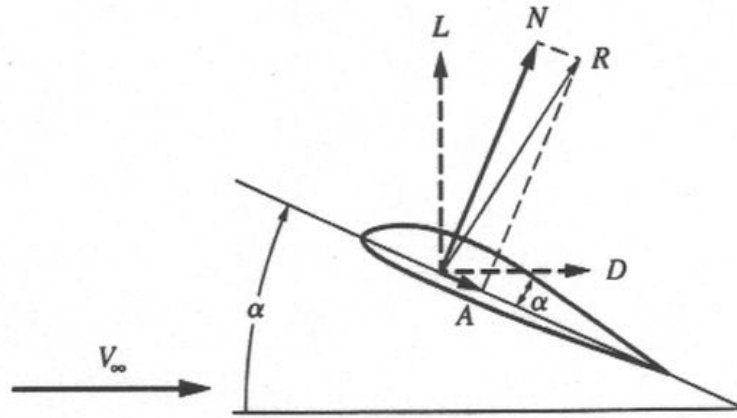
Figure 2.3: Aerodynamic Forces

- *Angle of Attack(α)*: Angle of the chord relative to the wind's direction.

- *Centerline*: line located equidistant of both tips following the fuselage.

- *x*: coordinate along the spam that has its origin is located at the centerline .

- *Root*: wing cross section at the centerline.

- *Tip*: wing cross section at the extremity of the wing

- *Span*: distance between the wing tips.

- *Taper*: ratio between the tip chord and the root chord.

- *Sweep (λ)*: angle of the leading edge in relation to the span.

In addition, to evaluate the performance of the airfoils herein analyzed, several aerodynamic concepts were utilized. The formal definition of these concepts are:

- *Cruise*: flight condition where altitude is stabilized. Time wise, it is the predominant flight condition. [**?**]

- *Landing*: flight condition where the aircraft descends from cruise altitude to the ground.

- *Resulting Force (R)*: it is the resultant force generated by wind pressure.

- *Lift (L)*: it is the component perpendicular to the wind's direction of R. As can be seen in Figure 2.3. High Lift is usually desirable. Aircraft's with higher lift can generate less drag, consume less fuel or carry more cargo.

- *Drag (D)*: it is the component perpendicular to the wind's direction of R. As can be seen in Figure 2.3. High drag for most flight conditions is undesirable. Since more thrust and, therefore, fuel, is necessary to propel the vehicle.

- *Pressure Coefficient*: It is the local unidimensional coefficient of the wind pressure. Since pressure along the airfoil surface varies, the coefficient is a local variable. If p_∞ and ρ are, respectively, the air pressure and density at the aircraft's altitude; and V_∞ the wind velocity; we have that:

$$C_p = \frac{p - p_\infty}{\rho V_\infty^2} \tag{2.1}$$

2.2 Aerodynamic loads: panel method

2.2.1 Panel method

AEROPY REFERENCE [19]

Although a free software known as Xfoil is utilized to calculate the aerodynamic pressures through the panel method, the author finds it necessary to introduce the theory behind the method to depict its advantages and disadvantages. This section is based on the lectures from Prof. Lorena A. Barba, author of the Aeropython lessons. [20]

The algorithm is initialized performing a discretization of the airfoil geometry into panels. The panel's attributes are: a starting point, an end point, a mid-point, its length and its orientation. Figure 2.4 depicts the nomenclature herein used.

Since the trailing and leading edge have more complicated geometries, the mesh needs to be more refined near these regions. For such, a standard method is to store the x-coordinate of the circle points to be the x-coordinate of the panel nodes, x, and project the y-coordinate of the circle points onto the airfoil by interpolation. We end up with a node distribution like this:

From potential flow theory, it is known that inviscid flows can be represented by the superposition of 5 elementary flow elements: a uniform flow, a vortex, a source, a sink and a doublet.

Figure 2.4: A single panel with its nomenclature
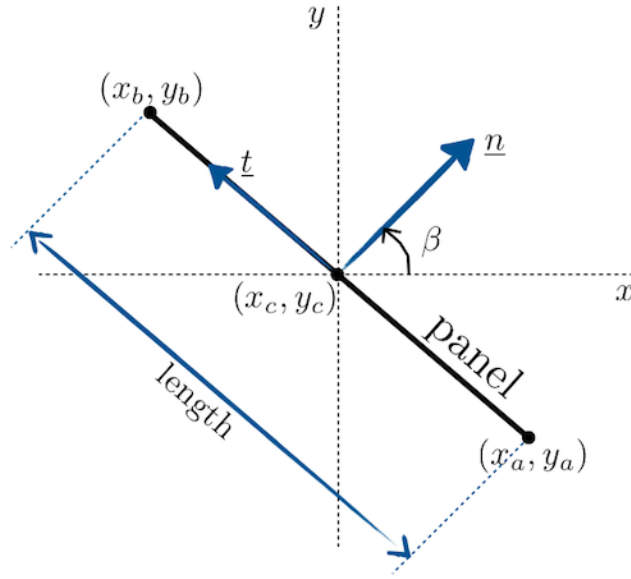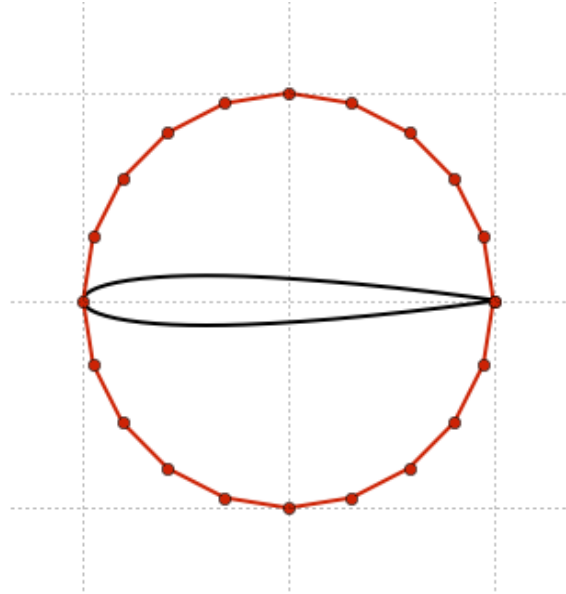

Figure 2.5: Outline of panels resulting from the circle method

Table 2.1: List of elementary flows

Uniform Flow:	$\phi = U_\infty + C$
Source (Sink):	$\phi = (-)\frac{\sigma}{2\pi} ln \left(\sqrt{(x_{c_i} - x_j(s_j))^2 + (y_{c_i} - y_j(s_j))^2} \right)$
Vortex:	$\phi = (-)\gamma tan^{-1} \left(\frac{y - y_{source}}{x - x_{source}} \right)$

If we consider a uniform flow at wind velocity U_∞, a source at the mid-point of each panel i and a vortexes of constant γ strength at each mid-point, using the principle of superposition, we have that the potential velocity is:

$$\phi\left(x_{c_i}, y_{c_i}\right) = U_\infty x_{c_i} \cos\alpha + U_\infty y_{c_i} \sin\alpha$$

$$+ \sum_{j=1}^{N} \frac{\sigma_j}{2\pi} \int_j \ln\left(\sqrt{(x_{c_i} - x_j(s_j))^2 + (y_{c_i} - y_j(s_j))^2}\right) \mathrm{d}s_j$$

$$- \sum_{j=1}^{N} \frac{\gamma}{2\pi} \int_j \tan^{-1}\left(\frac{y_{c_i} - y_j(s_j)}{x_{c_i} - x_j(s_j)}\right) \mathrm{d}s_j \tag{2.2}$$

Enforcing the flow-tangency condition on each panel mid-point (with subscript c) approximately makes the body geometry correspond to a dividing streamline (and the approximation improves if we represented the body with more and more panels). So, for each panel i, we make the component of u normal to the panel, $u_n =$, equal to zero at (x_{c_i}, y_{c_i}), that is

$$u_n = \frac{\partial}{\partial n_i}\left\{\phi\left(x_{c_i}, y_{c_i}\right)\right\} = 0 \tag{2.3}$$

which leads to:

$$0 = U_\infty \cos\left(\alpha - \beta_i\right) + \sum_{j=1}^{N} \frac{\sigma_j}{2\pi} \int_j \frac{\partial}{\partial n_i} \ln\left(\sqrt{(x_{c_i} - x_j(s_j))^2 + (y_{c_i} - y_j(s_j))^2}\right) \mathrm{d}s_j$$

$$- \sum_{j=1, j\neq i}^{N} \frac{\gamma}{2\pi} \int_j \frac{\partial}{\partial n_i} \tan^{-1}\left(\frac{y_{c_i} - y_j(s_j)}{x_{c_i} - x_j(s_j)}\right) \mathrm{d}s_j \tag{2.4}$$

where β_i is the angle that the panel's normal makes with the x-axis, so

$$\frac{\partial x_{c_i}}{\partial n_i} = \cos\beta_i \quad \text{and} \quad \frac{\partial y_{c_i}}{\partial n_i} = \sin\beta_i \tag{2.5}$$

and

$$x_j(s_j) = x_{a_j} - \sin\left(\beta_j\right) s_j$$
$$y_j(s_j) = y_{a_j} + \cos\left(\beta_j\right) s_j \tag{2.6}$$

But, there is still a problem to handle when i=j. So that the streamlines do not penetrate the panel, the source sheet strength should be equal to the incoming volume. Therefore, for an i-th panel to itself its contribution is $\frac{\sigma_i}{2}$. Applying the boundary condition at the center of the i-th panel on equation 2.4:

$$0 = U_\infty \cos\left(\alpha - \beta_i\right) + \frac{\sigma_i}{2}$$

$$+ \sum_{j=1, j \neq i}^{N} \frac{\sigma_j}{2\pi} \int_j \frac{\partial}{\partial n_i} \ln\left(\sqrt{(x_{c_i} - x_j(s_j))^2 + (y_{c_i} - y_j(s_j))^2}\right) \mathrm{d}s_j$$

$$- \sum_{j=1, j \neq i}^{N} \frac{\gamma}{2\pi} \int_j \frac{\partial}{\partial n_i} \tan^{-1}\left(\frac{y_{c_i} - y_j(s_j)}{x_{c_i} - x_j(s_j)}\right) \mathrm{d}s_j \tag{2.7}$$

Solving the partial derivations, we have that:

$$0 = U_\infty \cos\left(\alpha - \beta_i\right) + \frac{\sigma_i}{2}$$

$$+ \sum_{j=1, j \neq i}^{N} \frac{\sigma_j}{2\pi} \int_j \frac{(x_{c_i} - x_j)\frac{\partial x_{c_i}}{\partial n_i} + (y_{c_i} - y_j)\frac{\partial y_{c_i}}{\partial n_i}}{(x_{c_i} - x_j)^2 + (x_{c_i} - x_j)^2}) \mathrm{d}s_j$$

$$- \sum_{j=1, j \neq i}^{N} \frac{\gamma}{2\pi} \int_j \frac{(x_{c_i} - x_j)\frac{\partial y_{c_i}}{\partial n_i} - (y_{c_i} - y_j)\frac{\partial x_{c_i}}{\partial n_i}}{(x_{c_i} - x_j)^2 + (y_{c_i} - y_j)^2} \mathrm{d}s_j \tag{2.8}$$

The Kutta-condition states that the pressure below and above the airfoil trailing edge must be equal so that the flow does not bend around it, but leaves tangentially. The rear stagnation point must be exactly at the trailing edge. To enforce the Kutta-condition, we must include one more equation. We state that the pressure coefficient on the first panel must be equal to that on the last panel:

$$C_{p_1} = C_{p_N} \tag{2.9}$$

Using the definition of the pressure coefficient on a surface for an i-th panel:

$$C_{p_i} = 1 - \left(\frac{V_{t_i}}{U_\infty}\right)^2 \tag{2.10}$$

with equation 2.9 and considering that the horizontal axis of the coordinate system for both panels are inversed, we have that:

$$U_{t_1} = -U_{t_N} \tag{2.11}$$

Therefore, we need to evaluate the tangential velocity at the first and last panels. Let's derive it for every panel, since it will be useful to compute the pressure coefficient.

$$U_{t_i} = \frac{\partial}{\partial t_i}\left(\phi\left(x_{c_i}, y_{c_i}\right)\right) \tag{2.12}$$

9

i.e.,

$$U_{t_i} = U_\infty \sin(\alpha - \beta_i)$$

$$+ \sum_{j=1, j\neq i}^{N} \frac{\sigma_j}{2\pi} \int_j \frac{\partial}{\partial t_i} \ln\left(\sqrt{(x_{c_i} - x_j(s_j))^2 + (y_{c_i} - y_j(s_j))^2}\right) ds_j$$

$$- \sum_{j=1, j\neq i}^{N} \frac{\gamma}{2\pi} \int_j \frac{\partial}{\partial t_i} \tan^{-1}\left(\frac{y_{c_i} - y_j(s_j)}{x_{c_i} - x_j(s_j)}\right) ds_j \tag{2.13}$$

which gives

$$U_{t_i} = U_\infty \sin(\alpha - \beta_i)$$

$$+ \sum_{j=1, j\neq i}^{N} \frac{\sigma_j}{2\pi} \int_j \frac{(x_{c_i} - x_j)\frac{\partial x_{c_i}}{\partial t_i} + (y_{c_i} - y_j)\frac{\partial y_{c_i}}{\partial t_i}}{(x_{c_i} - x_j)^2 + (x_{c_i} - x_j)^2} ds_j$$

$$- \sum_{j=1, j\neq i}^{N} \frac{\gamma}{2\pi} \int_j \frac{(x_{c_i} - x_j)\frac{\partial y_{c_i}}{\partial t_i} - (y_{c_i} - y_j)\frac{\partial x_{c_i}}{\partial t_i}}{(x_{c_i} - x_j)^2 + (x_{c_i} - x_j)^2} ds_j \tag{2.14}$$

where $\frac{\partial x_{c_i}}{\partial t_i} = -\sin\beta_i$ and $\frac{\partial y_{c_i}}{\partial t_i} = \cos\beta_i$

Here, we build and solve the linear system of equations of the form:

$$[A][\sigma, \gamma] = [b] \tag{2.15}$$

where the $N+1 \times N+1$ matrix $[A]$ contains three blocks: an $N \times N$ source matrix (matrix $[S]$ in Equation 2.16), an $N \times 1$ vortex array to store the weight of the variable γ at each panel (vector $[g]$), and a $1 \times N+1$ Kutta array that represents our Kutta-condition (vector $[k]$).

$$S_{ij} = \begin{cases} \frac{1}{2} & \text{, if } i = j \\ \frac{1}{2\pi} \int \frac{(x_{c_i} - x_j(s_j))\cos\beta_i + (y_{c_i} - y_j(s_j))\sin\beta_i}{(x_{c_i} - x_j(s))^2 + (y_{c_i} - y_j(s))^2} ds_j & \text{, if } i \neq j \end{cases} \tag{2.16}$$

The right-hand-side vector b is defined as:

$$[b] = \begin{cases} b_i = -U_\infty \cos\beta_i & \text{, if } i \neq N+1 \\ b_{N+1} = -U_\infty \sin(\alpha - \beta_i) & \text{, if } i = N+1 \end{cases} \tag{2.17}$$

The main disadvantage of the Panel Method is the Paradox of D'Alembert , which states that for an incompressible and inviscid flow, the drag force is zero on a body moving with constant velocity relative to the fluid. Zero drag is in direct contradiction to the observation of substantial drag on bodies moving relative to fluids.[21] The solution adopted by the author of Xfoil, Mark Drela, is to apply the Squire-Young formula to obtain the Drag. The formula assumes that the wake
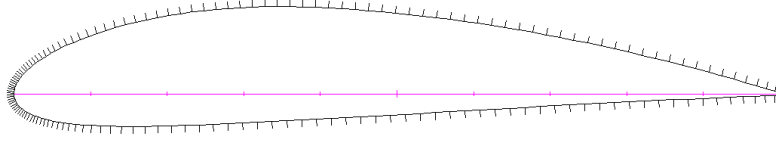
Figure 2.6: Panel distribution generated by Xfoil
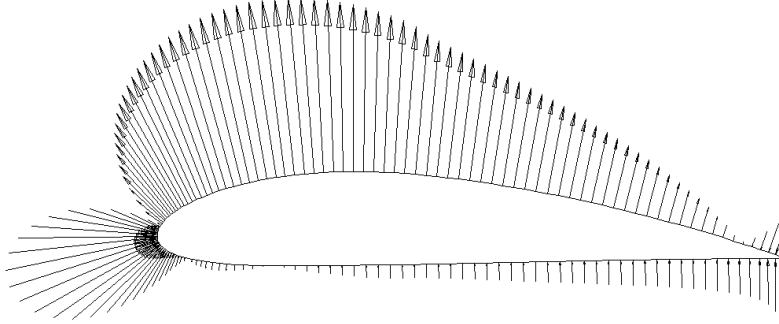
Figure 2.7: Pressure vectors generated by Xfoil

behaves in an asymptotic manner downstream of the point of application. This assumption is strongly violated in the near-wake behind an airfoil with trailing edge separation. Hence, the usual application of Squire-Young at the trailing edge is questionable with separation present, but its application for flow conditions before separation is reasonable. Therefore the problem of calculating aerodynamic pressures reduces to a linear algebric system. Wherein modern CFS's simulations would lead to much longer computational periods.

As mentioned before, instead of developing a Panel Method code, a free software is used. Xfoil was developed by Mark Drela from MIT and for the last two decades has been optimized. The concepts herein presented are applied in the software. It is able to generate panel meshes (Figure 2.6 and calculate the Pressure Coefficients (Figure 2.7)

For the dynamic modeling, the influence of the flow over the airfoil will take place via the moment generated by the air pressure on the flap in regards to the joint; hence it is necessary to: a) determine the surface of the flap in contact with the fluid at a given configuration; 2) calculate the moment coefficient for that configuration.

2.2.2 Determining flap surface

2.2.3 Moment coefficient

From Anderson [22] we have that for an inviscid fluid, the two-dimensional moment coefficient for a symmetric airfoil in regards to a given point, in this case the joint, is:

$$C_{m,J} = \frac{1}{c^2}\left[\int_0^c (C_{p,u} - C_{p,l})(x - x_J)dx + \int_o^c (C_{p,u} - C_{p,l})(y - y_J)dy\right] \quad (2.18)$$

where $C_{p,u}$ and $C_{p,l}$ are the pressure coefficients for the upper and lower surfaces, and c is the chord. Since the pressure coefficient values for a given set of coordinate $\{x, y\}$ on the airfoil surface is known, it is necessary to use *trapezoid rule*. For such it is convenient to define functions $f(x) = (C_{p,u} - C_{p,l})(x - x_J)$ and $g(y) = (C_{p,u} - C_{p,l})(y - y_J)$ so that we can rewrite **??** as:

$$C_{m,J} = \frac{1}{c^2}\left[\int_0^c f(x)dx + \int_o^c g(y)dy\right] \quad (2.19)$$

Therefore applying the trapezoid rule for both integrals in the coefficient and taking into consideration that the panel method indexation is counterclockwise and starts at the trailing edge (as such to have a positive Δx we subtract the x_i by x_{i+1}, not the contrary), we have that:

$$C_{m,J} = \frac{1}{c^2}\left[\sum_{i=0}^{n-1}\frac{f(x_i) + f(x_{i+1})}{2}(x_i - x_{i+1}) + \sum_{i=0}^{n-1}\frac{g(y_i) + g(y_{i+1})}{2}(y_{i+1} - y_i)\right]$$
$$(2.20)$$

Considering that $C_{p,u}^i = C_{p,u}(x_i) = C_{p,u}(y_i)$ and $C_{p,l}^i = C_{p,l}(x_i) = C_{p,l}(y_i)$, and that the minus sign from $C_{p,l}^i$ was substituted for a plus sign because the of coordinate system in the panel method $\Delta x = x_i - x_{i+1}$ will naturally become negative for the lower surface):

$$C_{m,J} = \frac{1}{2c^2}\left\{\sum_{i=0}^{n-1}\left[\left(C_{p,u}^i + C_{p,l}^i\right)(x_i - x_J) + \left(C_{p,u}^{i+1} + C_{p,l}^{i+1}\right)(x_{i+1} - x_J)\right](x_i - x_{i+1})\right.$$
$$\left. + \sum_{i=0}^{n-1}\left[\left(C_{p,u}^i + C_{p,l}^i\right)(y_i - y_J) + \left(C_{p,u}^{i+1} + C_{p,l}^{i+1}\right)(y_{i+1} - y_J)\right](y_i - y_{i+1})\right\}$$
$$(2.21)$$

2.3 Shape memory alloys

2.3.1 Overview and properties

Shape memory alloys (SMAs) are metallic alloys which undergo solid-to-solid phase transformations induced by the appropriate temperature and/or stress. The transformations are between 3 distinct crystalline structures: twinned martensite, de-twinned martensite and austenite [**?**]. Table 2.2 is summary of all of the characteristics of such alloys. The High Actuation Strain and the High Energy Density traits

Table 2.2: Summary of various SMA properties and their effects. [**?**]

| SMA Traits	Consequences
Shape Memory Effect	Material can be used as an actuator, providing force during shape recovery.
Pseudoelasticity	Material can be stressed to provide large, recoverable deformations at relatively constant stress levels.
Hysteresis	Allows for dissipation of energy during pseudoelastic response.
High Act. Stress (400-700MPa) [18, 74]	Small component cross-sections can provide substantial forces
High Act. Strain (8%) [18, 74]	Small component lengths can provide large displacements.
High Energy Density ($\sim$ 1200J/kg) [69]	Small amount of material required to provide substantial actuation work.
Three-Dimensional Actuation	Polycrystalline SMA components fabricated in a variety of shapes, providing a variety of useful geometric configurations
Actuation Frequency	Difficulty of quickly cooling components limits use in high frequency applications.
Energy Efficiency (10%–15%) [69]	Amount of thermal energy required for actuation is much larger than mechanical work output.
Transformation-Induced Plasticity	Plastic accumulation during cyclic response eventually degrades material and leads to failure.
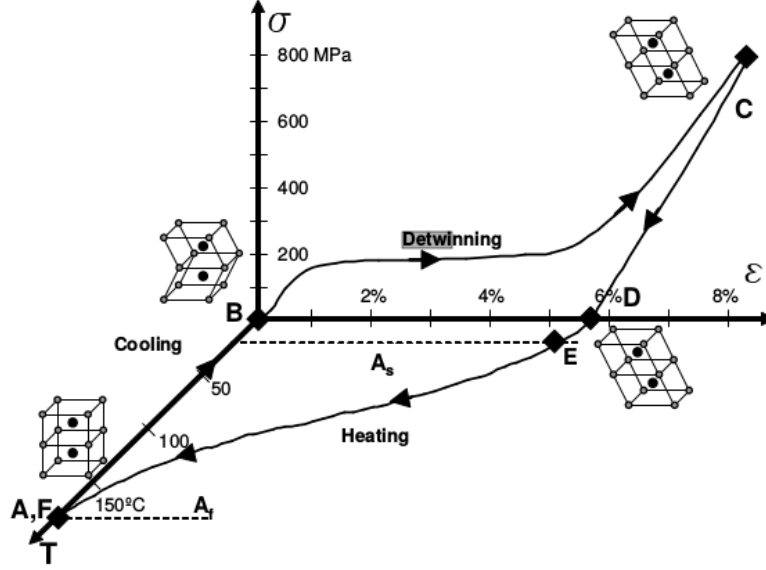
Figure 2.8: Shape Memory Effect

are the main reason why SMAs are of interest to the Aerospace industry. Hence, the reason why this kind of material was here selected. Each phase transformation has a pre-defined start and final temperature, where the martensite fraction can vary from 0 (pure austenite) to 1 (pure martensite). The transformation between the pure states are known as martensite transformation (from 0 to 1) and austenite transformation (from 1 to 0).

The primary characteristic of these alloys is the *Shape Memory Effect* depicted in Figure 2.8. If the alloy is in a twinned martensite state, e.g. no stress and $T < A_s$, where A_s is the temperature where austenitization starts, when loaded above σ_{Ms}, martensite starts to be detwinned. Once $\sigma > \sigma_{Mf}$, martensite is complety detwinned and returns to elastically deform. When unloaded a residual strain is noticeable since the material is still in detwinned martensite state. To recover to its original form, the material is heated above A_f, the temperature where the austenite transformation is complete, recovering the residual strain. This highly coupled thermal-mechanical behaviour is of great interest for actuation purposes.

From Figure 2.9, one can notice that the transformation temperatures from Austenite to Martensite (M_s and M_f) and from Martensite to Austenite (A_s and A_f) are different. This results in a behaviour known as a hysteresis depicted in Figure 2.10, which is the result of an energy dissipation.

Another phenomena characteristic to SMAs is the *Pseudoelastic effect*. The transformation from austenite to detwinned martensite, stress-induced, can generate reversible inelastic strains. The strains are recovered once the load are reduced to their original values. An experimental evidence of such effect can be observed on Figure 2.11.
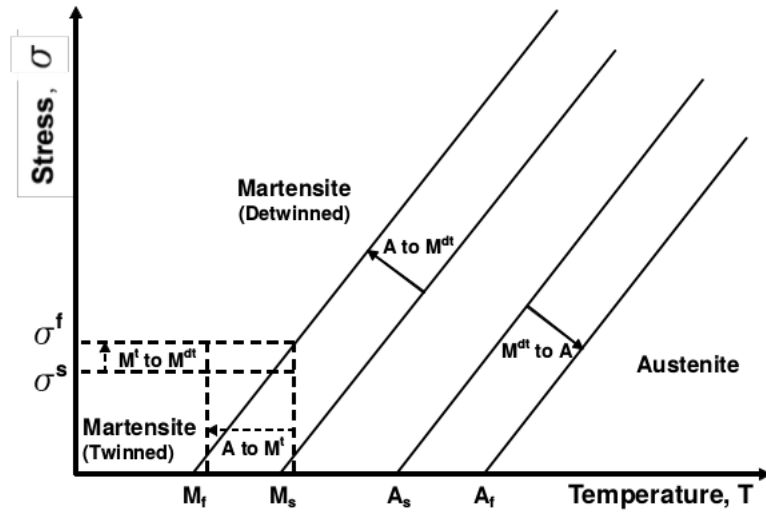
14

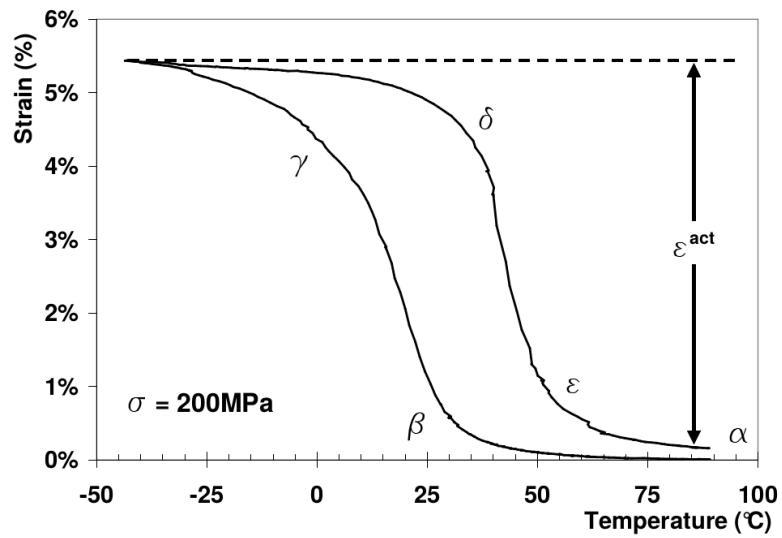Figure 2.9: SMA stress-temperature phase diagram (schematic) [?]

Figure 2.10: Experimental results illustrating the SMA under a constant 200MPa stress [?]
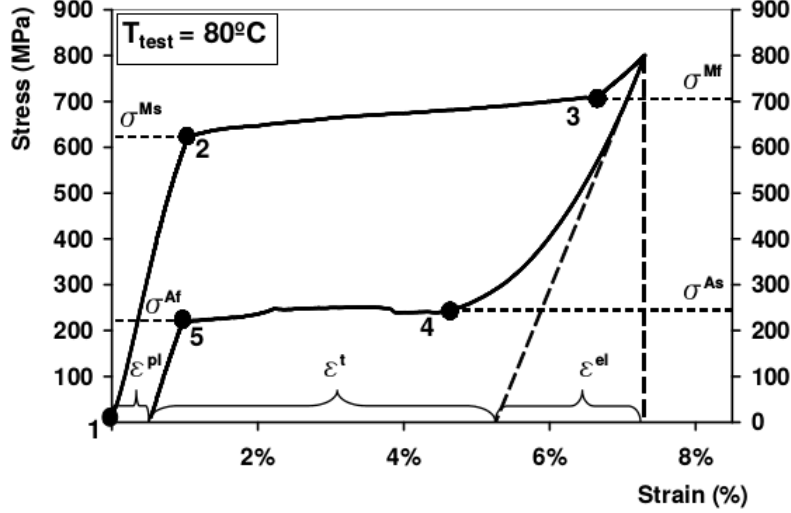
Figure 2.11: Experimental result depicting the Pseudoelastic Effect [**?**]

2.3.2 Thermal-mechanical modeling

NEED TO FIX EXPLANATION, NOT HELMHOLTZ FREE ENERGY

The thermo-mechanical behavior of SMAs can be described by constitutive models that establish a phenomenological description of these alloys. Herein, the Hartl-Lagoudas [**?**] model is employed. Contrary to other method, martensitic transformation is not considered. Only the generation and recovery of transformation strains that occur as a result of martensitic transformation is taken into account. The model considers three external state variables: the stress σ, the total strain ϵ, and the absolute temperature T. Two internal state variables are also considered: the inelastic transformation strain ϵ^t (e.g. caused by transformation) and the martensitic volume fraction ξ. The model follows the Helmholts free energy principle, therefore the temperature and the total strain are assumed to be known. Additive decomposition is assumed by considering elastic, thermal and inelastic contributions.

$$\epsilon = \mathbf{S}(\xi)\sigma + \alpha(T - T_o) + \epsilon^t \tag{2.22}$$

where $\mathbf{S}(\xi)$ is the phase-dependent fourth-order compliance tensor, written as

$$\mathbf{S}(\xi) = \mathbf{S}^A - \xi(\mathbf{S}^A - \mathbf{S}^M) = \mathbf{S}^A - \xi\tilde{\mathbf{S}} \tag{2.23}$$

where $\mathbf{S}^A$ and $\mathbf{S}^M$ are the compliance tensors for austenitic and martensitic phases, respectively; α is the second-order coefficient of thermal expansion tensor, where T_o is the material reference temperature. Standard isotropic forms are assumed for $\mathbf{S}(\xi)$ and α, and they are computed from material properties to be described shortly.

The inelastic transformation strain evolves such that the time rate of change of

both its magnitude and direction are given as

$$\dot{\epsilon}^t = \dot{\xi} \begin{cases} H^{cur}(\bar{\sigma}\frac{3\sigma'}{2\bar{\sigma}}) & ; \dot{\xi} > 0 \\ \frac{\epsilon^{t-r}}{\xi^r} & ; \dot{\xi} < 0 \end{cases} \tag{2.24}$$

During forward transformation ($\dot{\xi} > 0$), the formulation for the direction of transformation follows the assumptions of classical associative Mises plasticity. The Mises equivalent stress is given as $\bar{\sigma} = \sqrt[2]{3/2\sigma' : \sigma'}$, where σ' is the deviatoric stress. The magnitude of transformation strain generated during full martensite transformation is captured by the scalar-valued function $H^{cur}(\bar{\sigma})$. For trained materials, H^{cur} may be considered as follows:

$$H^{cur}(\sigma) = \begin{cases} H_{min} & ; \bar{\sigma} \leq \sigma_{crit} \\ H_{min} + (H_{max} - H_{min})(1 - \exp^{-k(\sigma - \sigma_{crit})}) & ; \sigma > \sigma_{crit} \end{cases} \tag{2.25}$$

here H_{min}, H_{max}, k and $\bar{\sigma}_{crit}$ are model parameters.

During reverse transformation ($\dot{\xi} < 0$), the direction and magnitudes are defined such that all transformation strain existing at the cessation of austenite transformation (i.e., at which time $\xi \to \xi^r$ and $\epsilon^t \to \epsilon^{t-r}$) is fully recovered should the material transform fully back into austenite. Having related stress, total strain, and inelastic strain, and further having defined an evolution equation for the inelastic strain ϵ^t, we need only define constraints on the evolution of the martensitic volume fraction ξ, which acts as a scalar multiplier in 2.24. For this purpose, we introduce the transformation function Φ. Inspired by the methods of classical plasticity, the following constraints are stated:

$$\Phi^t \leq 0, \quad \dot{\xi}\Phi^t = 0, \quad 0 \leq \xi \leq 1 \tag{2.26}$$

where the first two represent the the Kuhn-Tucker constraints (e.g. first order conditions for a solution of a nonlinear problem to be optimal), and the third bounds the martensitic volume fraction, which naturally ranges from 0 to 1.

From the definition 2.24, we have that forward and reverse transformation are distinctive process, therefore

$$\Phi^t = \begin{cases} \Phi^t_{fwd} & ; \dot{\xi} \geq 0 \text{ and } 0 \leq \xi < 1 \\ \Phi^t_{rev} & ; \dot{\xi} < 0 \text{ and } 0 \leq \xi < 1 \end{cases} \tag{2.27}$$

Φ^t_{fwd} and Φ^t_{rev} are given by

$$\Phi^t_{fwd} = (1 - D)H^{cur}(\bar{\sigma})\bar{\sigma} - \frac{1}{2}\sigma : \tilde{\mathbf{S}}\sigma - \rho\Delta s_o T + \rho\Delta u_o$$
$$- \left[\frac{1}{2}a_1(1 + \xi^{n_1} + (1 - \xi)^{n_2}) + a_3\right] - Y^t_o \qquad (2.28)$$

$$\Phi^t_{rev} = (D - 1)\frac{\sigma : \epsilon^{t-r}}{\xi^r} + \frac{1}{2}\sigma : \Delta\mathbf{S}\sigma + \rho\Delta s_o T + \rho\Delta u_o$$
$$- \left[\frac{1}{2}a_2(1 + \xi^{n_3} + (1 - \xi)^{n_4}) + a_3\right] - Y^t_o \qquad (2.29)$$

where D and T^t_o are transformation dissipation parameters; $\rho\Delta s_o$ and $\rho\Delta u_o$ are the volume-specific change in reference to entropy and to internal energy between martensite and austenite, respectively; a_1, a_2 and a_3 are transformation hardening coefficients while n_1, n_2, n_3 and n_4 are transformation hardening exponents.

2.3.3 Thermal-mechanical-electrical model

The thermo-mechanical behavior of SMAs can be described by constitutive models that establish a phenomenological description of these alloys. Herein, the Hartl-Lagoudas [1] model is employed. The model considers three external state variables: the stress σ, the total strain ϵ, and the absolute temperature T. Two internal state variables are also considered: the inelastic transformation strain ϵ^t (e.g. caused by transformation) and the martensitic volume fraction ξ. The model is derived by postulating a Gibbs free energy potential and assumed elastic domain in the seven stress-temperature hyperspace. A through explanation of the the Constitutive Model can be found in the work of Lagoudas et al.[1]

For minimizing the energy (i.e. voltage) utilized by the SMA mechanism, the electrical resistivity, ρ, must be known. Since the electrical resistance of shape memory alloys is dependant of several factors [23], it was necessary to consider certain simplifications and to couple it to the thermal-mechanical Hart-Lagoudas model. For the temperature range between 20^oC to 100^oC, it is typical to use the linear approximations in equations 2.30 for ρ [24], where α^A_ρ and α^M_ρ are the variation coefficients; and T^A_o and T^M_o are the temperatures at which the resistivity were measured. This approximation for SMA components is supported by experimental results.[25, 26] Based on the works from M. Pozzi and G. Airoldi [26] and Gonzalez et al. [25], the martensite and austenite electrical resistivity, ρ_M and ρ_A, at a given temperature are further assumed to be functions of stress. Considering that ρ is coupled via the martensite volume fraction as a result of a mixture law between

Thermoelastic properties		Phase diagram properties	
E_A (MPa)	44420	A_f (K)	367
E_M (MPa)	31628	A_s (K)	342
ν_A	0.33	M_f (K)	302.15
ν_M	0.33	M_s (K)	327
α_A (1/K)	0	C_A (MPa/K)	9.522
α_M (1/K)	0	C_M (MPa/K)	8.623
Transformation strain properties		Transformation hardening coefficients	
$H^{\max}$	0.0405	n_1	0.618
$H^{\min}$	0	n_2	0.313
k (1/MPa)	0.391	n_3	0.759
σ_{crit} (Pa)	0	n_4	0.358
ρ (kg/m^3)		6450	

Table 2.3: Material properties for a shape memory alloy [**?**]

both micro-structures resistivity, equation 2.31 characterizes the resistivity of shape memory alloys.

$$\rho^A(T,\sigma) = \rho^A(\sigma, T = T_o)[1 + \alpha_\rho^A(T - T_o^A)] \quad \rho^M(T,\sigma) = \rho^A(\sigma, T = T_o)[1 + \alpha_\rho^M(T - T_o^M)] \tag{2.30}$$

$$\rho(T,\sigma) = \rho^A(T,\sigma) + \xi(T,\sigma)[\rho^M(T,\sigma) - \rho^A(T,\sigma)] \tag{2.31}$$

The thermal properties are obtained through differential scanning calorimetry (DSC). INSTRON equipment is used for performing tensile tests to measure mechanical properties. A similar set-up of Gonzalez et al.(2004) is used for measuring the electrical properties. The INSTRON equipment is used for controlling stress. An Arduino is used for controlling the voltage and measuring temperature and current.

The work from Mirzaeifar et al.[27] has shown that good results can be obtained for an Abaqus model of a 3D SMA spring model utilizing UMAT subroutines. An electrical-thermal subroutine (UMATHT) applying equation 2.31 within the framework of Abaqus FEA is developed. An electrical-thermal-mechanical simulation for a 3D SMA spring is undertaken by simultaneously using the UMATHT and the Lagoudas et al.[1] thermal-mechanical subroutine (UMAT). Because of computational cost, the 3D model will act as a validation for the 1D model used for this optimization.

Thermoelastic properties		Phase diagram properties	
E_A (GPa)	33	A_f (K)	370
E_M (GPa)	33	A_s (K)	274
ν_A	0.33	M_f (K)	220
ν_M	0.33	M_s (K)	333
α_A (1/K)	1.0E-5	C_A (MPa/K)	9.522
α_M (1/K)	1.0E-5	C_M (MPa/K)	8.623
Transformation strain properties		Transformation hardening coefficients	
$H^{\max}$	0.047	n_1	0.6
$H^{\min}$	0.007	n_2	0.6
k (1/MPa)	0.391	n_3	0.6
σ_{crit} (Pa)	140 MPa	n_4	0.6

Table 2.4: Material properties for a shape memory alloy [1]

2.3.4 Material properties

2.4 Optimization

2.4.1 OpenMDAO

> Update for the new OpenMDAO.

OpenMDAO is an open Multidisciplinary Design Analysis and Optimization platform [?]. Developed by NASA and written in Python. It's purpose is to facilitate the communication between 3rd party softwares in working environment where other features such as optimization or design of experiments can be easily implemented. Such a framework is possible due to the separation of the flow of information, *dataflow*, from the process in which analyses are executed, *workflow*. The software is composed of four specific constructs. They are:

- *Component*: an object with input and output variables. It can be a wrapped 3rd party software or a code written by the user (in python or any other language). It is possible to have multiple components that communicate with each other.

- *Assembly*: a group of linked *components* with a specified dataflow between them.

- *Driver*: responsible for iterating over a workflow until some condition is met such as in an optimization or a design of experiments.

- *Workflow*: responsible for dictating the components to execute and in that order to execute them for a given driver. Drivers can also be used inside a workflow, enabling nested iterations.

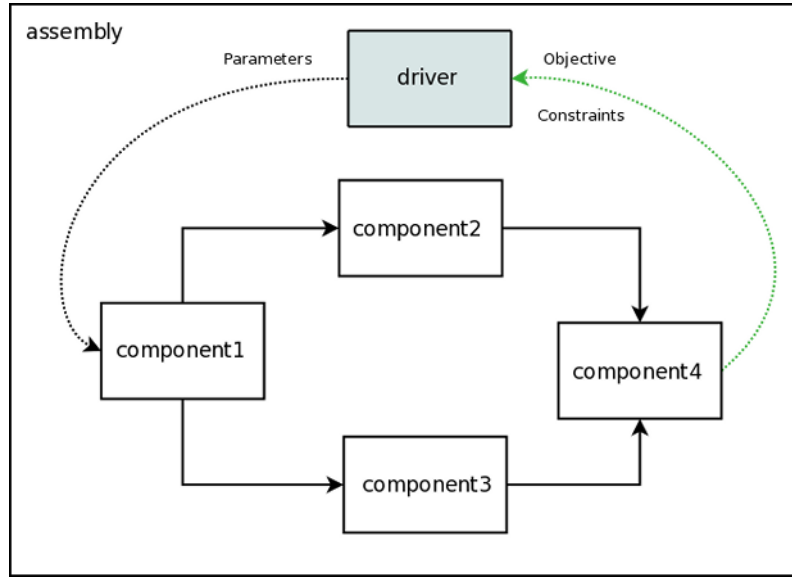An overview of an usual OpenMDAO framework utilizing the above constructs is depicted in Figure 2.4.1.

Figure 2.12: View of an Assembly Showing Data Flow

2.4.2 NGSAII

Update this section in case not NSGAII algorithm

Since heuristic methods become increasingly more effective in finding the global optimum given a large number of design variables and considering also the expected high degree of non-linearity in the design response, for this work a robust and efficient genetic algorithm known as NSGA-II (Non Sorting Genetic Algorithm II) [?] was selected for all optimizations. This well known option is included in the current distribution of OpenMDAO. In such a scheme, each design variable is treated as a gene; a combination of these genes represents the chromosome of an individual design; a group of individuals is treated as a population. Techniques inspired by natural evolution, such as crossovers, mutations and natural selection, generate a series of design population generations that should eventually include the nearly optimal solution.

Find actual reference of this image

The procedure of the NSGA-II, depicted in Figure 2.13 is as follows:

1. *Population Initialization*: based on the population size, N, and ranges defined by the user, the population is created (R_0)

2. *Non-Dominated sort*: as in any genetic algorithm, every individual p is evaluated (i.e maximum Von Mises Stress, tip displacement) and therefore attributed a fitness. However a non-dominated sort also considers the set the
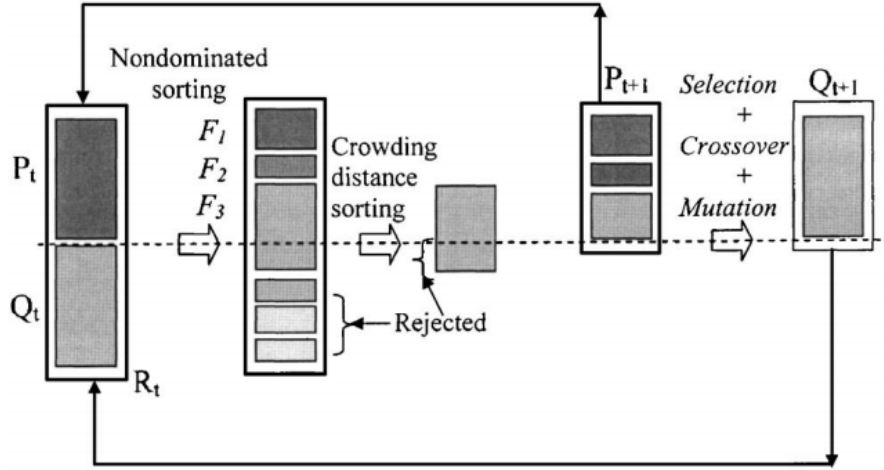
Figure 2.13: Schematic of NSGA-II algorithm

individual dominates (S_p) and the number of individuals that dominate the individual (n_p), organizing the population in to fronts, F_i. All individuals in front F_1 have fitness 1, in front F_2 have fitness 2 and so on. Once all individuals are sorted, the individuals with higher fitness are rejected. If M is the number of individuals in the set P_t of surviving configurations, individuals in fronts with fitness higher that that of the M-th sorted individual are rejected.

3. *Crowding Distance*: is the measure of how close an individual is to the individuals in it's own front. Large average crowding distance will result in better diversity in the population. The population in each front is sorted according to it's crowding distance. Individuals of the highest front with crowding distance lower than that of the M-th sorted individual are rejected. The result is set P_{t+1}, the pool of possible candidates.

4. *Genetic Operators*: inspired by natural evolution, three algorithms are used to generate new individuals of set Q_{t+1}, the *offspring*:

   - *Binary Tournament Selection*: two randomly chosen individuals are drawn from the P_{t+1}. An individual is selected if the fitness is lesser than the other, and if the fitness are equal, the individual is selected if crowding distance is greater than the other.

   - *Binary Crossover*: generation of individuals through random interpolation of the genes of two individual's from P_{t+1}.

   - *Mutation*: to avoid local minimums, a genetic algorithm is utilized. It enables variation of genes even when the results has converged, hence the global minimum in the domain can be found if enough generations are .

5. *Recombination*: *elitism* The offspring population of the previous step is combined with the current generation population and selection is performed to set the individuals of the next generation resulting in set R_{t+1}. Since all the previous and current best individuals are added in the population, *elitism* is ensured. If by adding all the individuals in F_i the population exceeds N then individuals in F_i are selected based on their crowding distance in the descending order until the population size is N. And hence the process repeats starting from step 2 onwards until the user defined number of generations is reached.

Chapter 3

Static modeling

A 2D FEA flap model was developed, but due to the low stresses at the flap compo-
nents, it was further simplified such that these components can be modeled as rigid
bodies; hence this work herein utilized dynamic modeling.

Each actuator, e.g. linear spring or SMA wire, is dynamically described in the
same fashion. Figure 3.1 shows that each end of an actuator is fixed on a different
rigid body, one at the forwards component (point $-$) and one at the afterwards
component (point $+$). The two rigid bodies are connected at the joint point J.

Before developing the dynamic equations, it is necessary to define the reference
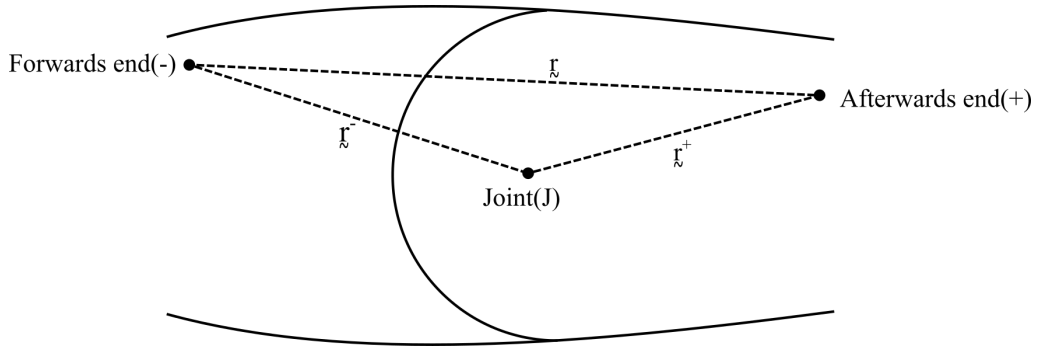systems as in table 3.1.

Forwards end(-) $\underset{\sim}{r}$ Afterwards end(+)

$\underset{\sim}{r}^{-}$ $\underset{\sim}{r}^{+}$

Joint(J)

Figure 3.1: Schematic of a single actuator

Notation	Reference system	Origin
R_0	Inertial reference system	joint 1: J_1
R_1	Rotational reference system of first flap	joint 1: J_1
R_i	Rotational reference system of first flap	joint i: J_i

Table 3.1: Reference systems

3.1 Direct solution

This section is quite similar to the work done by Faria [28]. Following the notation of Ilmar [29], the length vectors are described as:

$$
{}_{R_0}\mathbf{r}^- = \begin{pmatrix} x^- \\ y^- \\ 0 \end{pmatrix} \quad
{}_{R_1}\mathbf{r}^+ = \begin{pmatrix} x^+ \\ y^+ \\ 0 \end{pmatrix} \quad
{}_{R_0}\mathbf{r} = \begin{pmatrix} x_r \\ y_y \\ 0 \end{pmatrix} = {}_{R_0}\mathbf{r}_+ - {}_{R_0}\mathbf{r}_- \quad (3.1)
$$

If θ_i is the rotation angle around point J_i and $\{x_{J_i}, y_{J_i}, 0\}$ are coordinates of the the same point, we have that the transformation between both reference systems is depicted by the following operator:

$$
{}_{R_0}T_{R_1} = \begin{vmatrix} cos\theta & -sin\theta & 0 \\ sin\theta & cos\theta & 0 \\ 0 & 0 & 1 \end{vmatrix} \quad (3.2)
$$

$$
{}_{R_0}\mathbf{a} = {}_{R_0}T_{R_1\,R_1}\mathbf{a} = \begin{vmatrix} cos\theta & -sin\theta & 0 \\ sin\theta & cos\theta & 0 \\ 0 & 0 & 1 \end{vmatrix} \begin{pmatrix} x^+ \\ y^+ \\ 0 \end{pmatrix} = \begin{pmatrix} x^+ cos\theta - y^+ sin\theta \\ x^+ sin\theta + y^+ cos\theta \\ 0 \end{pmatrix} \quad (3.3)
$$

Then from equation 3.1 we have that the distance vector $\mathbf{r}$ can be rewriten as:

$$
{}_{R_0}\mathbf{r} = \begin{pmatrix} x^+ cos\theta - y^+ sin\theta - x^- \\ x^+ sin\theta + y^+ cos\theta - y^- \\ 0 \end{pmatrix} \quad (3.4)
$$

3.2 Inverse solution

If it is known that the length of the actuator, $\mathbf{r}$, undergoes a deformation η (or $1 + \epsilon$ if ϵ is strain), it is necessary to calculate the resultant angle θ by solving the
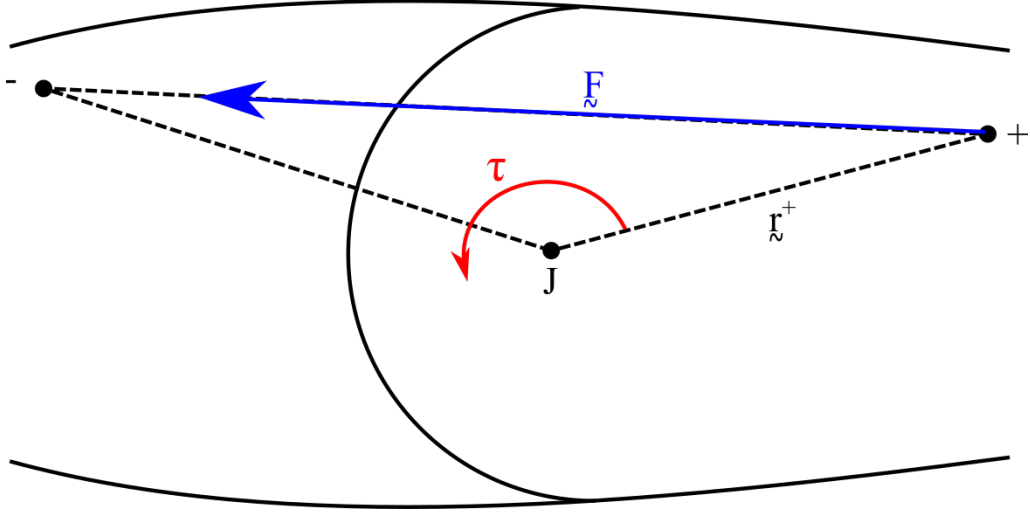
following system:

$$\eta x_{r0} = x^+ cos\theta - y^+ sin\theta - x^- \tag{3.5}$$

$$\eta y_{r0} = x^+ sin\theta + y^+ cos\theta - y^- \tag{3.6}$$

which the solution is:

$$\theta = atan2(sin\theta, cos\theta) \tag{3.7}$$

where atan2 is a function that calculates the arctangent taking in to consideration the signs of the inputs in order to return the appropriate quadrant of the computed angle, and

$$cos\theta = \frac{\eta y_{r0} + y^- + (\eta x_{r0} + x^-)x^+/y^+}{y^+ + x^{+2}/y^+} \tag{3.8}$$

$$sin\theta = \frac{-\eta x_{r0} - x^- + x^+ cos\theta}{y^+} \tag{3.9}$$

If there is an initial strain ϵ_o:

$$\eta = 1 + \epsilon_{total} - \epsilon_o \tag{3.10}$$

$$\mathbf{r}_o =) (\tag{3.11}$$

3.3 Torque generated by one actuator

The torque generated by each actuator is:

$$\tau = {}_{R_0}\mathbf{r}^+ \times \mathbf{F} = (a_1 cos\theta - a_2 sin\theta)F_2 - (a_1 sin\theta + a_2 cos\theta)F_1 \tag{3.12}$$

where

$$\mathbf{F} = F\frac{R_0\mathbf{r}}{||\mathbf{r}||} \tag{3.13}$$

Therefore

$$\tau = \frac{F}{||\mathbf{r}||}\left[(x^+cos\theta - y^+sin\theta)y_{r0} - (x^+sin\theta + y^+cos\theta)x_{r0}\right] \tag{3.14}$$

F will be defined in the following section.

3.4   Angular momentum equilibrium at origin

Denoting the shape memory alloy actuators with subscript $_s$, linear actuators with subscript $_l$ and the weight with subscript $_w$, we have that

$$\tau_s + \tau_l + \tau_w = 0 \tag{3.15}$$

where (W is a scalar that depicts the aircraft weight)

$$\tau_w = r_wWcos\theta \tag{3.16}$$

Substituting

$$\begin{aligned}
0 =& \frac{F^s}{||\mathbf{r}^s||}\left[(x_s^+cos\theta - y_s^+sin\theta)y_{r0}^s - (x_s^+sin\theta + y_s^+cos\theta)x_{r0}^s\right] \\
&+ \frac{F^l}{||\mathbf{r}^l||}\left[(x_l^+cos\theta - y_l^+sin\theta)y_{r0}^l - (x_l^+sin\theta + y_l^+cos\theta)x_{r0}^l\right] \\
&+ x_w^+Wcos\theta
\end{aligned}$$

If the dynamic simulation is force/stress-driven we have that

$$\begin{aligned}
F^s =& \frac{||\mathbf{r}^s||}{(x_s^+sin\theta + y_s^+cos\theta)x_{r0}^s - (x_s^+cos\theta - y_s^+sin\theta)y_{r0}^s}\{\frac{F^l}{||\mathbf{r}^l||}\left[(x_l^+cos\theta - y_l^+sin\theta)y_{r0}^l - (x_l^+sin\theta + y_l^+cos\right. \\
&+ r_wWcos\theta\}
\end{aligned} \tag{3.17}$$

Otherwise, if the simulation if strain-driven

$$\begin{aligned}
F^l =& \frac{||\mathbf{r}^l||}{(x_l^+sin\theta + y_l^+cos\theta)x_{r0}^l - (x_l^+cos\theta - y_l^+sin\theta)y_{r0}^l}\{\frac{F^s}{||\mathbf{r}^s||}\left[(x_s^+cos\theta - y_s^+sin\theta)y_{r0}^s - (x_s^+sin\theta + y_s^+cos\right. \\
&+ r_wWcos\theta\}
\end{aligned}$$

Since $F^l = ku = k\epsilon^l ||\mathbf{r}^l||$,

$$\epsilon^l = \frac{1/k}{(x_l^+ sin\theta + y_l^+ cos\theta)x_{r0}^l - (x_l^+ cos\theta - y_l^+ sin\theta)y_{r0}^l} \times$$
$$\left\{ \frac{F^s}{||\mathbf{r}^s||} \left[(x_s^+ cos\theta - y_s^+ sin\theta)y_{r0}^s - (x_s^+ sin\theta + y_s^+ cos\theta)x_{r0}^s \right] + r_w W cos\theta \right\} \quad (3.18)$$

3.5 Initial conditions

At initial conditions, $\theta = 0$, the temperature is below transformation temperature; hence it is expected that the shape memory alloy actuator will be fully martensitic. Considering the initial pre-stress as a design variable, from the relation of transformation strain in function of stress (equation 2.25), we have that for $\sigma_o^s > \sigma_{crit}$:

$$\epsilon_o^t = H_{min} + (H_{max} - H_{min})(1 - \exp^{-k(\sigma_o^s - \sigma_{crit})}) \quad (3.19)$$

Since, this main objective of this work is the development of a reusable actuator device, it is necessary that after heating the SMA actuator, the original configuration is attained after cooling. Therefore, it is necessary that the linear actuator to provide sufficient stress to fully detwinne the martensitic actuator at θ_0. Figure 3.2 describes how the detwinning process takes place. Since a fully detwinned martensite has linear elastic properties, $\epsilon_o^s = \frac{E_M}{\sigma_o^s}$, we have that the the initial total strain is:

$$\epsilon_o^s = \frac{\sigma_o^s}{E_M} + \epsilon_o^t \quad (3.20)$$

The initial elastic strain is calculated via equation 3.18, where $F^s = \sigma_o^s A^s$.

Since the SMA is a wire, it is easy to change the actuator length. Therefore, we have that the length of the wire is such that it provides the required strainϵ_o^s, hence:

$$l^s = \frac{||r^s||}{1 + \epsilon_o^s} \quad (3.21)$$

Whereas for the linear spring, there is not a great flexibility for the actuator length. Nevertheless, with the use of a mechanism to deter the flap moving upwards at the initial configuration, it suffices that the moment generated by the linear actuator is equal or higher than the designed moment. Therefore, the elastic deformation

$$\epsilon_o^l|_{actual} = \frac{||r^l||}{l^l} - 1 \geq \epsilon_o^l|_{designed} \quad (3.22)$$
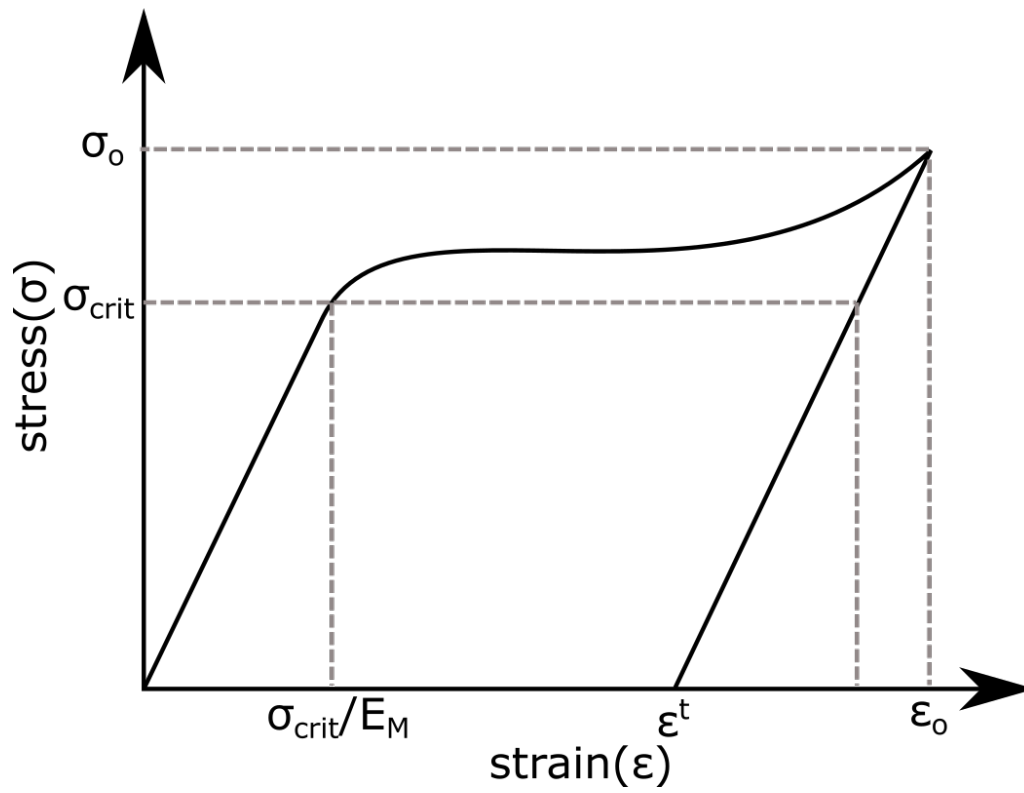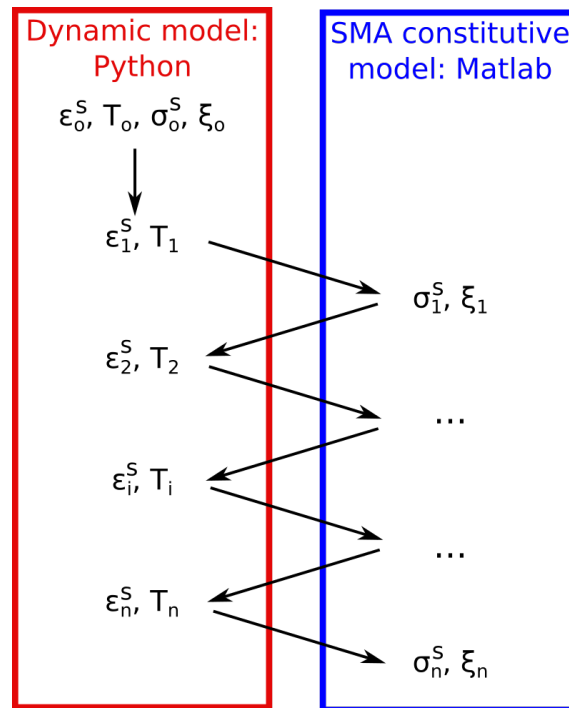
3.6 Aplication

28

Figure 3.2: Pre-strain

Chapter 4

Dynamic modeling

Chapter 5

Experimental setup

5.1 Experimental characterization

5.1.1 Thermal characterization

5.1.2 Thermal-mechanical characterization

5.1.3 Thermal-electrical-mechanical characterization

5.1.4 Pytables database

5.2 Experimental apparatus

5.2.1 Model itself

5.2.2 Sensors

Chapter 6

Conclusion

asd

Bibliography

[1] D. Lagoudas, D. Hartl, Y. Chemisky, L. Machado, and P. Popov, "Constitutive model for the numerical analysis of phase transformation in polycrystalline shape memory alloys," *International Journal of Plasticity*, vol. 32-33, pp. 155–183, May 2012.

[2] D. Lagoudas, *Shape memory alloys: modeling and engineering applications*. New York: Springer, 1st ed ed., 2008.

[3] D. J. Hartl and D. C. Lagoudas, "Aerospace applications of shape memory alloys," *Proceedings of the Institution of Mechanical Engineers, Part G: Journal of Aerospace Engineering*, vol. 221, pp. 535–552, Jan. 2007.

[4] M. A. Savi, A. Paiva, A. P. Baeta-Neves, and P. M. C. L. Pacheco, "Phenomenological Modeling and Numerical Simulation of Shape Memory Alloys: A Thermo-Plastic-Phase Transformation Coupled Model," *Journal of Intelligent Material Systems and Structures*, vol. 13, pp. 261–273, May 2002.

[5] J. Valasek, ed., *Morphing aerospace vehicles and structures*. AIAA progress series, Reston, VA: John Wiley & Sons, 2012.

[6] S. Barbarino, E. I. Saavedra Flores, R. M. Ajaj, I. Dayyani, and M. I. Friswell, "A review on shape memory alloys with applications to morphing aircraft," *Smart Materials and Structures*, vol. 23, p. 063001, June 2014.

[7] M. Senthilkumar, "Analysis of SMA Actuated Plain Flap Wing," *Journal of Engineering Science and Technology Review*, vol. 5, no. 1, pp. 39–43, 2012.

[8] J. N. Kudva, "Overview of the DARPA Smart Wing Project," *Journal of Intelligent Materials Systems and Structures*, vol. 15, pp. 261–267, Apr. 2004.

[9] G. Song and N. Ma, "Robust control of a shape memory alloy wire actuated flap," *Smart Materials and Structures*, vol. 16, pp. N51–N57, Dec. 2007.

[10] G. Song, B. Kelly, and B. N. Agrawal, "Active position control of a shape memory alloy wire actuated composite beam," *Smart Materials and Structures*, vol. 9, no. 5, p. 711, 2000.

[11] S. Enemark, M. A. Savi, and I. F. Santos, "Nonlinear dynamics of a pseudoelastic shape memory alloy system - theory and experiment," *Smart Materials and Structures*, vol. 23, Aug. 2014.

[12] Q. A. Donnelan, "Design and testing of linear shape memory alloy actuator," *Final Report, National Science Foundation–Research Experience for Undergraduates*, 2005.

[13] K. Ikuta, M. Tsukamoto, and S. Hirose, "Shape memory alloy servo actuator system with electric resistance feedback and application for active endoscope," in , *1988 IEEE International Conference on Robotics and Automation, 1988. Proceedings*, pp. 427–430 vol.1, Apr. 1988.

[14] S. Kayama and Y. Kataoka, "Drive unit using shape memory alloy," June 2002. U.S. Classification 310/307; International Classification E05B47/00, F03G7/06, H01H13/20; Cooperative Classification F03G7/06, F16F2224/0258; European Classification F03G7/06.

[15] K. K. Jee, "Actuator using shape memory alloy," Jan. 2014. U.S. Classification 60/527; International Classification F03G7/06; Cooperative Classification F03G7/065.

[16] A. Bellini, M. Colli, and E. Dragoni, "Mechatronic Design of a Shape Memory Alloy Actuator for Automotive Tumble Flaps: A Case Study," *IEEE Transactions on Industrial Electronics*, vol. 56, pp. 2644–2656, July 2009.

[17] D. K. Schmidt, *Modern flight dynamics*. New York, NY: McGraw-Hill, 2012.

[18] R. G. Budynas, J. K. Nisbett, and J. E. Shigley, *Shigley's mechanical engineering design*. Mcgraw-Hill series in mechanical engineering, New York, NY: McGraw-Hill Education, tenth edition ed., 2015.

[19] P. Camara Leal, "AeroPy," Feb. 2016.

[20] L. Barba, "AeroPython," 2014.

[21] G. Falkovich, *Fluid mechanics: a short course for physicists*. Cambridge ; New York: Cambridge University Press, 2011.

[22] J. D. Anderson, *Fundamentals of aerodynamics*. Anderson series, New York: McGraw-Hill, 5th ed ed., 2011.

[23] N. Ma, G. Song, and H.-J. Lee, "Position control of shape memory alloy actuators with internal electrical resistance feedback using neural networks," *Smart Materials and Structures*, vol. 13, pp. 777–783, Aug. 2004.

[24] M. Ward, *Electrical Engineering Science.* McGraw-Hill, 1971.

[25] C. H. Gonzalez, N. F. d. Quadros, C. J. d. Araújo, M. Morin, and G. Guénin, "Coupled stress-strain and electrical resistivity measurements on copper based shape memory single crystals," *Materials Research*, vol. 7, no. 2, pp. 305–311, 2004.

[26] M. Pozzi and G. Airoldi, "The electrical transport properties of shape memory alloys," (Santa Clara, Calif), SMST, 1999.

[27] R. Mirzaeifar, R. DesRoches, and A. Yavari, "A combined analytical, numerical, and experimental study of shape-memory-alloy helical springs," *International Journal of Solids and Structures*, vol. 48, pp. 611–624, Feb. 2011.

[28] C. T. d. Faria, "Controle da variação do arqueamento de um aerofólio utilizando atuadores de memória de forma," 2010.

[29] I. F. Santos, *Dinâmica de sistemas mecânicos: modelagem, simulação, visualização, verificação.* São Paulo: Makron, 2001.